Final Draft
of the original manuscript:

Srinivasan, P.B.; Kumar, S.:
Microstructural and electrochemical characterization of a thin-section dissimilar stainless steel weld joint
In: Materials Chemistry and Physics (2009) Elsevier

DOI: 10.1016/j.matchemphys.2008.11.044

Microstructural and electrochemical characterization of a thin-section dissimilar stainless steel weld joint

P. Bala Srinivasan[1,] *, M.P. Satish Kumar[2]

[1]Institute of Materials Research
GKSS-Forschungszentrum Geesthacht GmbH
D 21502, Geesthacht, Germany

[2]Mabani Steel, Ras Al Khaimah
United Arab Emirates

*Corresponding Author
Email: bala.srinivasan@gkss.de ;
Phone: 00-49-4152-871997; Fax: 00-49-4152-871909

Abstract
A dissimilar weld joint consisting of an austenitic stainless steel (ASS) and a martensitic stainless steel (MSS) was obtained under optimized welding conditions by autogenous gas tungsten arc welding technique. The weld metal was found to be dual-phased, and was constituted with an austenite matrix containing interdendritic ferrite of about 3 – 8 EFN, with over-matching mechanical properties. Electrochemical behaviour assessment of the composite zone comprising the weld metal, HAZ of both ASS and MSS showed different general corrosion behaviour in neutral and acidic chloride solutions. However, in both the electrolytes, the pitting susceptibility of this region was the highest, and the MSSHAZ of this composite zone was the observed to be more vulnerable to the localized damage.

Keywords
Dissimilar weld; Stainless steels; Microstructure; Hardness; Corrosion behaviour.

Introduction
Joining of dissimilar materials for meeting the industrial requirements has widely been attempted in the last two decades, employing both fusion and solid state welding processes [1-4]. Excellent mechanical properties combined with corrosion

resistance make stainless steels as candidates, even today, for many of the demanding engineering applications. Even though studies on the structure property correlations in weld joints of a variety of stainless steels have widely been taken up and documented **[5-8]**, the research data available on the dissimilar stainless steel combinations is very limited **[9-10]**. Some of the major issues concerning the joining of dissimilar stainless steels include: (a) selection of appropriate fillers in the case of thick section joints, (b) pile-up of residual stresses due to differences in thermal expansion coefficients of materials, (c) development of structures with different electrochemical potentials/behaviour as a result of joining etc., **[11-12]**. In the case thin-section steels, welding is generally done by autogenous gas tungsten arc welding (GTAW) and in recent times power beam processes viz. laser and electron beam welding are also contemplated **[13-15]**. As there are potential applications in the nuclear and aerospace sectors for the employment of dissimilar joints, an attempt has been made in this work to understand the microstructural evolution in a dissimilar weld joint comprising an austenitic stainless steel and a martensitic stainless steel by employing autogenous GTAW. The resultant weldment was characterized for the micro hardness, and the electrochemical behaviour of the different regions of this weldment was assessed by potentiodynamic polarisation studies in neutral and acidic chloride solutions to characterize the general and pitting corrosion behaviour.

Experimental

A martensitic stainless steel (MSS) corresponding to AISI 410 and an austenitic stainless steel (ASS) of AISI 316 grade of 1.5 mm thickness were employed in this investigation. Two coupons of size 250 mm x 75 mm, one each from MSS and ASS, were joined together by autogenous single-pass gas tungsten arc welding

(GTAW) with a square-butt weld configuration employing back hand welding technique. Argon gas of 99.9% purity level was used as a shielding gas and also as back purging gas (to avoid oxidation at the root region) with flow levels of 18 – 20 liters per minute and 10 – 14 liters per minute, respectively. The following welding parameters were optimized based on preliminary experiments and were employed for obtaining the final welds for this investigation: Current: 70 – 75 A; Voltage: 14 – 16 V; Welding speed: 140 – 160 mm/min, Tungsten electrode diameter: 2.5 mm.

Specimens for metallographic observation were prepared by polishing successively in 220, 320, 400, 800 and 1200 grit emery sheets followed by final polishing in 0.5 μm diamond paste slurry. Etching of the weld metal and the ASS parent metal was carried out electrolytically in a 10% oxalic acid solution and the MSS side was swab-etched with Vilella's reagent. Microstructural characterisation was done in a Leitz light optical microscope. Micro hardness survey was performed in a Zwick Vickers micro hardness tester under a load of 5 N with a loading dwell time of 20s. Ferrite content assessment was done using a Fischer Feritscope.

The electrochemical studies were performed using a flat cell with 8 mm diameter opening for the exposure of specimen surface (with a corresponding surface area of 0.5 cm^2) and the tests were performed in a Gill AC potentiostat/galvanostat. Since the weld bead obtained was narrow (~4 mm wide), the corrosion behaviour of the weld metal/HAZ regions of ASS/MSS was assessed as 'composite zone'. A three electrode cell was employed for the corrosion studies, in which the specimen, saturated calomel electrode and a platinum electrode were made as working, reference and auxiliary electrodes, respectively. Corrosion tests were performed in neutral chloride solutions of different concentrations (0.01M, 0.1M, 0.5M and 1M NaCl) and also in 1M sulphuric acid solution with different

concentrations of chloride (0.1M, 0.5M and 1M NaCl) using specimens prepared to metallographic finish as described earlier. The specimens were cleaned with acetone before the electrochemical experiments. Experiments were performed at room temperature (30±2°C) and in triplicate for each condition to ascertain the reproducibility, at a sweep rate of 0.5 mV s^{-1}. The specimens after the electrochemical experiments were examined in a Hitachi scanning electron microscope to assess the corrosion damage on the tested surfaces.

Results and Discussion

Microstructure

Figures 1(a) and (b) show the microstructural features of the ASS and MSS parent metals, respectively. A banded structure characteristic of rolled product is seen in ASS and the polygonal grains with twins are also visible. On the other hand, the martensitic stainless steel in the annealed condition showed equiaxed ferrite grains and dispersed carbides in a ferrite matrix.

The interface between the MSS and the weld metal in this dissimilar weldment shown in **Figure 2** reveals the type II boundary. The development of type II boundary due to composition differences have been reported in literature **[16-17]**. The heat affected zone (HAZ) in the MSS close to the fusion boundary had a coarse martensitic structure, apparently on account of coarsening of austenite in the HAZ and consequent transformation into coarse martensite upon cooling. Also, a fine martensitic structure was noticed next to this zone in the region towards the parent alloy. In contrast, the interface between the ASS and the weld metal had developed different features, as could be noticed in **Figure 3**. Close to the fusion boundary, the ASS region consisted of a narrow zone (< 100 μm) of fine dendrites of ferrite and austenite. The weld metal close to this fusion boundary had a cellular structure, which was different from that observed in the MSS side. This

suggests that there could be compositional differences in these two regions, and the mode of solidification could have also been different. However, the compositional analysis could not be carried out as EDX/EPMA facility was not available. The microstructural features of the weld metal, observed in the regions 200 μm from the fusion boundary of ASS and MSS sides, are depicted in **Figures 4(a) and (b)**, respectively. Even though close to the fusion boundary the microstructures were distinctly different, the morphological feature in the rest of the regions of this weld metal was more or less similar.

Ferrite content

Assuming an equal level of dilution from the ASS and MSS parent metals, the ferrite content of this autogenous weld metal was predicted using WRC-1992 and is depicted in **Figure 5**. Based on the Cr and Ni equivalence values, the ferrite level was calculated to be in the range 2 – 4 EFN for the weld metal. The ferrite content was assessed using a Fischer Feritscope as extended ferrite number (EFN). In the ASS parent and MSS parent regions, ferrite contents of 0.5 EFN and 132 EFN, respectively, were registered. On the other hand, in the weld metal the ferrite level was in the range of 3 – 8 EFN, corroborating the predictions made using WRC diagram. Interestingly, in the HAZ region of MSS ferrite contents in the range of 85 – 95 EFN was observed, and it was surprising to note that this region with a martensitic structure, though magnetic in nature as like ferritic structure, with similar chemical composition of the MSS parent alloy did register a lower value. The exact reasons for this are not clearly understood at this point of time; however, the observations suggest that the Feritscope can be used as a non-destructive tool for understanding the martensitic transformation on a quantitative scale.

Microhardness

The MSS parent metal showed a hardness of around 170 $HV_{0.5}$ despite the fact that the carbides are dispersed in the matrix. However, the softness is attributed to the completely ferritic structure from the annealing treatment received by this material. The ASS parent also had a similar hardness of around 170 $HV_{0.5}$. The weld metal region registered hardness values in the range of 360 $HV_{0.5}$ – 370 $HV_{0.5}$, which was surprising. It is difficult to comprehend the reasons for the development of such high hardness levels in the weld metal region, as it is constituted essentially of austenite with very small amounts of ferrite. Microscopic examination revealed the absence of martensite in this region, and this was further ascertained by ferrite content measurements. Had there been any martensite in the weld metal, then one would have expected EFN values much higher than those observed/reported here. A representative microstructure of the weld metal region **(Figure 6)**, close to the ASS fusion boundary showing only a two phase structure, reveals the differences in the hardness in the WM, and HAZ/parent of ASS. J.R. Berretta et. al., have reported the development of weld metals with a higher hardness in the dissimilar welds comprising AISI 304 and AISI 420 stainless steels **[18]**. They did not comment on the microstructural features of the weld metal, and instead had attributed the higher hardness to the higher cooling rates associated with laser welding, also to the position of the beam.

The micro hardness survey made across this dissimilar weldment is depicted in **Figure 7**. The hardness in the ASS side was more or less the same, registering around 170 $HV_{0.5}$ and no HAZ was noticed. No carbide precipitation was noticed in the HAZ of the ASS and this is possibly on account of controlled heat input levels employed during welding. In the MSS side, in the HAZ regions with coarse

and fine martensite a hardness value of around 370 $HV_{0.5}$ was observed, and the HAZ width was of the order of 1 mm – 2 mm in the MSS side. The above data suggests that the weld metal of this dissimilar weldment is over-matched in terms of hardness. In the transverse tensile tests, performed in duplicate, fracture occurred in the MSS parent metal, suggesting that this region in the annealed state was the weakest section in the joint and this further reaffirms the over-matched nature of the weld metal.

Electrochemical behaviour

The potentiodynamic polarisation behaviour of the ASS and MSS parent metals and the "composite" weld metal/HAZ region of this dissimilar weldment in neutral sodium chloride solution of different concentrations are shown in **Figures 8 (a), (b)** and **(c)**, respectively. The corrosion potential of the ASS parent region was around -235 $\pm$ 5 mV vs. SCE in NaCl solution of different concentrations, ranging from 0.01 M to 1 M and the corrosion current density values were nearly the same, registering around 0.20 µA cm^{-2} in all the electrolytes. In the case of MSS, the corrosion potential was observed to drift towards the active side with increase in chloride concentration, especially in 0.5 M and 1 M solutions. Further, the corrosion current densities were much higher for the MSS parent region in 0.5 M and 1 N NaCl solutions, registering values of 0.98 µA cm^{-2} and 1.86 µA cm^{-2}, respectively. On the other hand, the composite region consisting of the weld metal, HAZ of MSS and HAZ of ASS, surprisingly, showed corrosion potentials and current density levels similar to that observed for the ASS parent region. The breakdown potentials for the ASS parent region in chloride solutions were found to decrease with increase in concentration, as can be seen from Figure 8. The pitting behaviour of the composite zone comprising the weld metal, HAZ of ASS and MSS was similar to that of the MSS parent alloy. Examination of this specimen after the polarisation tests revealed the presence of pits only in the MSS HAZ

region and the other two regions (weld metal and ASS HAZ) were free from pits. This indicates the higher susceptibility of MSS HAZ region in all the electrolytes containing different chlorides levels.

The potentiodynamic polarisation behaviour of the ASS and MSS parent metals and the weld metal/HAZ region of this dissimilar weldment in 1M H_2SO_4 solution and with different chloride concentrations are shown in **Figures 9 (a), (b)** and **(c)**, respectively. The corrosion potential of the ASS parent region was around -150 mV vs. SCE in solution containing 0.01 M NaCl, and it drifted towards the active side with increase in chloride concentration, registering a value of -350 mV vs. SCE in the 1 M sulphuric acid containing 1 M NaCl and the critical current density increased with increase in chloride level. Only in the solution containing 1 M NaCl breakdown/pitting was noticed in ASS, and in this solution the passivation current density was also higher compared to that in the rest of the test solutions. Even though the weld metal/HAZ region showed a better general corrosion resistance in neutral chloride solution (matching that of the ASS parent metal), the corrosion behaviour of this composite region in 1M sulphuric acid containing different levels of chloride ions has been observed to be highly inferior to that of the ASS parent. A closer examination and analysis of the polarisation plots revealed that in terms of pitting resistance and passivation behaviour, the weld metal/HAZ region showed nearly similar performance to that of the MSS region. Not only the corrosion potentials were very active (around -500 mV vs. SCE) for these specimens, but in terms of corrosion current density, passivation current density and breakdown potential also the behaviour was inferior to that of the ASS parent. This inferior corrosion resistance in these relatively aggressive electrolytes can be attributed to be lower levels chromium, and also the absence of molybdenum and nickel in the MSS parent.

Optical macrograph of the composite specimen comprising the weld metal/HAZ, subjected to polarisation test in 1M sulphuric acid containing 1M NaCl depicted in **Figure 10** bring out some interesting features. It appears that the dissolution of the material was more in the MSS side, as could be observed from the ditch structure in the macrograph, and this augments the observation that the potential and current density values were close to that observed for the MSS parent. The scanning electron micrograph showing the pits in the ASS parent metal after the polarisation test in 1 M sulphuric acid containing 1 M sodium chloride is shown in **Figure 11(a)** and the higher magnification micrograph of the pit is presented in **Figure 11(b)**. The pits were observed to be deep and in addition the presence of numerous tiny pits could also be noticed in the higher magnification micrograph. The scanning electron micrograph of the composite weld metal/HAZ region in the MSS side after polarisation in the aforementioned electrolyte shown in **Figure 12(a)** reveals the higher degree dissolution of the MSS region, exemplified by the step like structure at the MSS-WM interface. The weld metal and the ASS did seem to undergo uniform dissolution, and the representative micrograph shown in **Figure 13** illustrates the uniform dissolution of these regions. A comparison of this micrograph with Figure 11(b) reveals the extent of localized damage in these regions, and it is plausibly on account of the preferential dissolution of the MSS region in this composite weldment specimen. The above observations suggest that the weld metal/HAZ region of this weldment is susceptible to corrosion attack, and the HAZ region of the MSS is highly vulnerable to localized corrosion damage as like the MSS parent.

Conclusions

Weld joints comprising MSS and ASS can successfully be accomplished without the problems of cracking, with weld metals having a dual phased structure and over-matched mechanical properties. In terms of corrosion behaviour, the

composite region comprising the weld metal/ASSHAZ/MSSHAZ was found to be highly susceptible to pitting corrosion in neutral chloride solution similar to the MSS parent alloy. In acidic chloride solutions, despite having a distinctly different microstructural feature, the dissolution and pitting behaviour of the composite region was nearly the same as that of the MSS parent alloy, and the MSSHAZ portion of the composite region was found to be the vulnerable region for the corrosion damage.

Acknowledgement

The authors thankfully acknowledge the support of the management of M/s GB Engineering Enterprises Private Limited, Tiruchirappalli for extending the services of qualified welders and the GTAW facility for the welding experiments.

References

[1] A. Celik, A. Alsaran, Materials Characterization, 43 (1999) 311.

[2] S. Katayama S, Welding International,18 (2004) 618.

[3] I. Shigematsu, Y. J. Kwon, K. Suzuki, T. Imai, N. Saito, Journal of Materials Science Letters, 22 (2003) 353.

[4] Y. Li, L.E. Murr, J.C. McClure, Scripta Materialia, 40 (1999) 1041.

[5] V. Muthupandi, P. Bala Srinivasan, S.K. Seshadri, S. Sundaresan, Materials Science and Engineering, A358 (2003) 9.

[6] M. Dadfar, M. H. Fathi, F. Karimzadeh, M. R. Dadfar, A. Saatchi: Materials Letters, 61 (2007) 2343.

[7] Y. Cui, C. D. Lundin, V. Hariharan: Journal of Materials Processing and Technology, 171 (2006) 150.

[8] S. K. Samantha, S. K. Mitra, T. K. Pal, Materials Science and Engineering, A430 (2006) 242.

[9] R. Kocar, O. Baylan, Materials and Design, 25 (2004) 317.

[10] V. V. Satyanararayana, G. M. Reddy, T. Mohandas, Journal of Materials Processing and Technology, 16 (2005) 128.

[11] C. D. Lundin, Welding Journal, 61 (1982) 58s.

[12] M. Sireesha, V. Shankar, S. K. Albert, S. Sundaresan: Materials Science and Engineering, A292 (2000) 74.

[13] M.P. Satish Kumar, P. Bala Srinivasan, Materials Letters, 62 (2008) 2887.

[14] Y.-C. Liao, M.-H. Yu, Journal of Materials Processing and Technology, 190 (2007) 102.

[15] V. Muthupandi, P. Bala Srinivasan, V. Shankar, S.K. Seshadri, S. Sundaresan, Materials Letters, 59 (2005) 2305.

[16] T.W. Nelson, J.C. Lippold, M.J. Mills, Welding Journal, 78 (1999) 329s.

[17] M.D. Rowe, T.W. Nelson, J.C. Lippold, Welding Journal, 78 (1999) 31s.

[18] J. R. Berretta, W. de Rossi, M. D. Martins das Neves, I. A de Almeida, N. D. Viera, Optics and Lasers in Engineering, 45 (2007) 960.

Figure captions

Figure 1 Optical micrographs of ASS and MSS parent metals

Figure 2 Optical micrograph of the weld metal-MSS interface showing type II and fusion boundaries

Figure 3 Optical micrographs showing the fusion boundary in ASS side

Figure 4 Optical micrograph of the weld metal at two different locations

Figure 5 WRC-1992 diagram for the prediction of ferrite content in MSS-ASS dissimilar weldment (Arrow indicates the predicted ferrite content)

Figure 6 Optical micrograph showing hardness indentations in the weld metal, interface and ASS side of the weldment

Figure 7 Micro hardness profile across the ASS-MSS dissimilar weldment

Figure 8 Potentiodynamic polarization plots of parent ASS, MSS and ASS-weld-MSS (composite) regions in chloride solutions

Figure 9 Potentiodynamic polarization plots of parent ASS, MSS and ASS-weld-MSS (composite) regions in 1M H_2SO_4 solution containing different concentrations of NaCl

Figure 10 Optical macrograph of the weld metal/HAZ specimen subjected to polarisation in 1M H_2SO_4 acid containing 1M NaCl

Figure 11 Scanning electron micrographs showing the pit morphology in ASS parent metal (after polarisation in 1M H_2SO_4 acid containing 1M NaCl)
(a) Lower magnification (b) Higher magnification

Figure 12 Scanning electron micrograph showing the corrosion damage at the interface between the MSS and weld metal (after polarisation in 1M H_2SO_4 acid containing 1M NaCl)

Figure 13 Scanning electron micrograph showing the corrosion damage in the weld metal (after polarisation in 1M H_2SO_4 acid containing 1M NaCl)

Figure 1a
Click here to download high resolution image

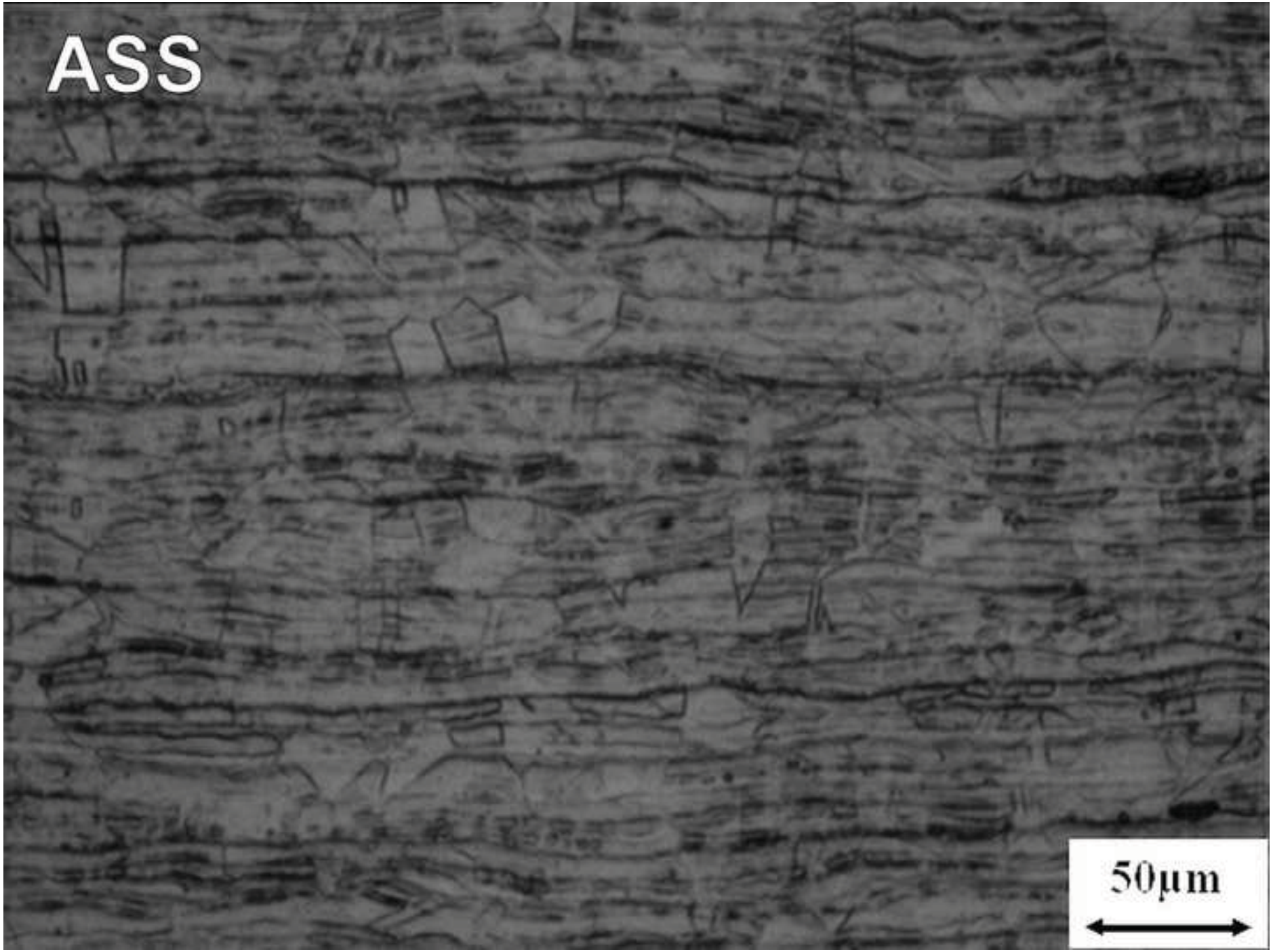

Figure 1b
Click here to download high resolution image

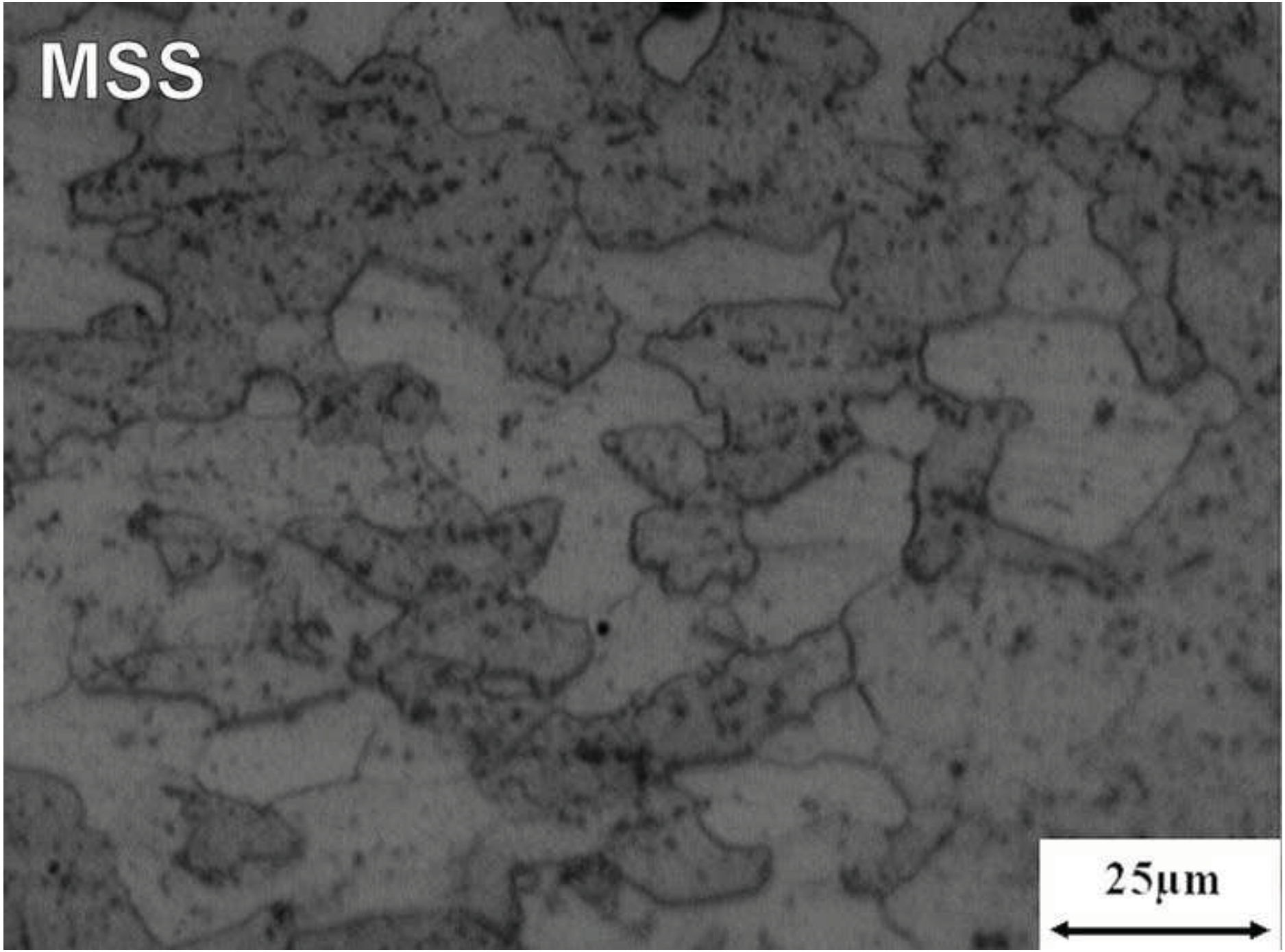

Figure 2
Click here to download high resolution image

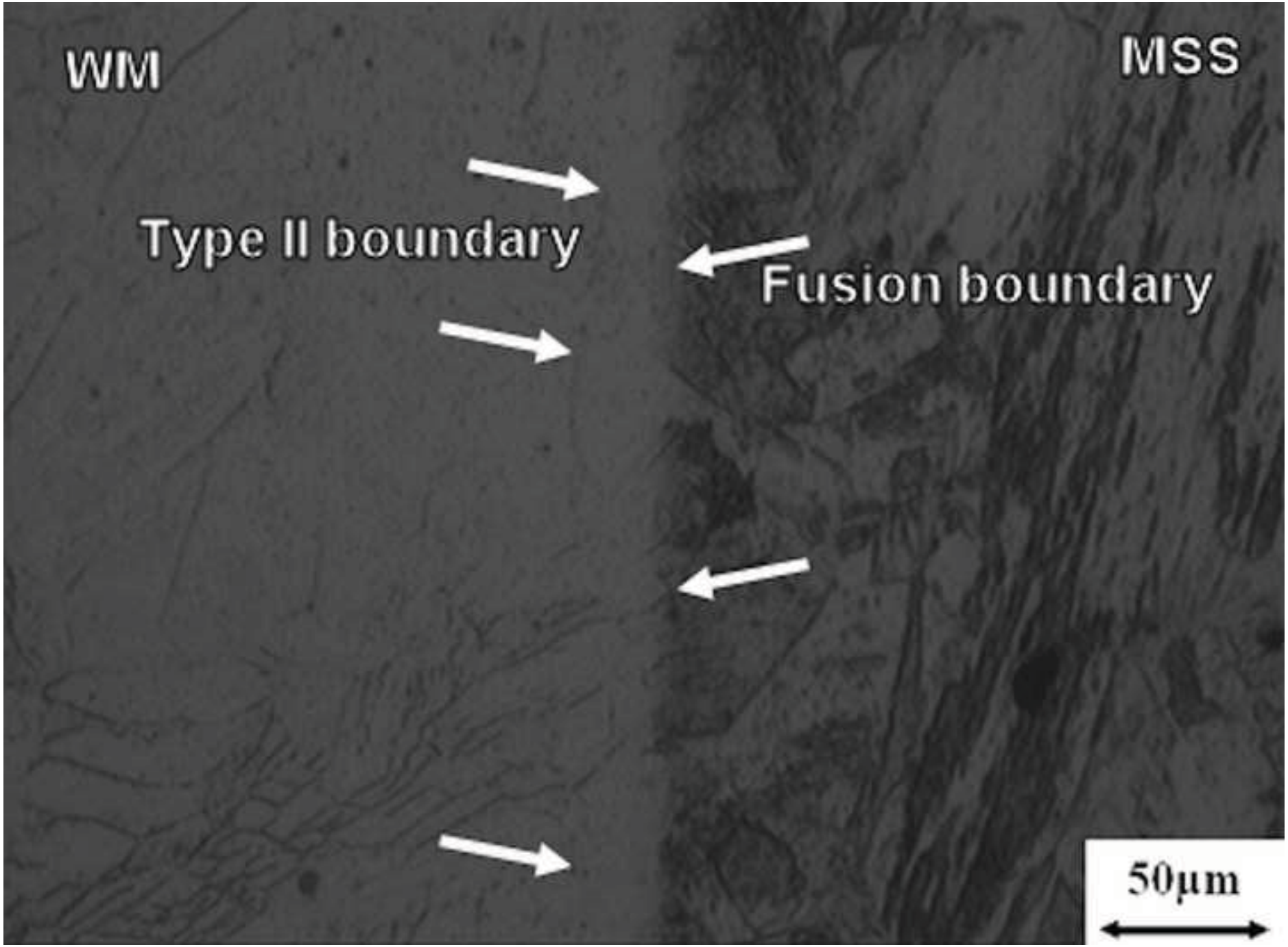

Figure 3

Click here to download high resolution image

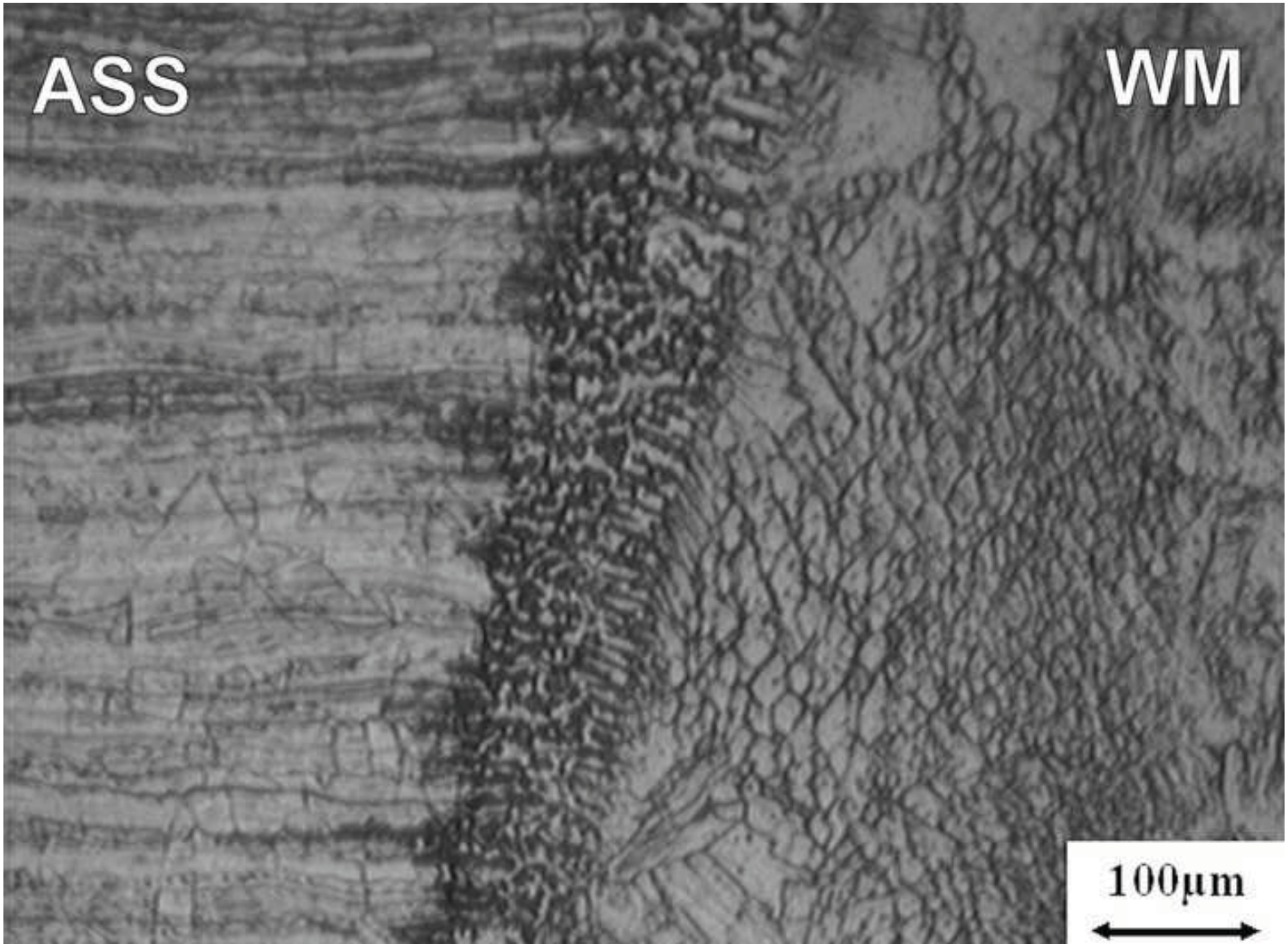

Figure 4a
Click here to download high resolution image

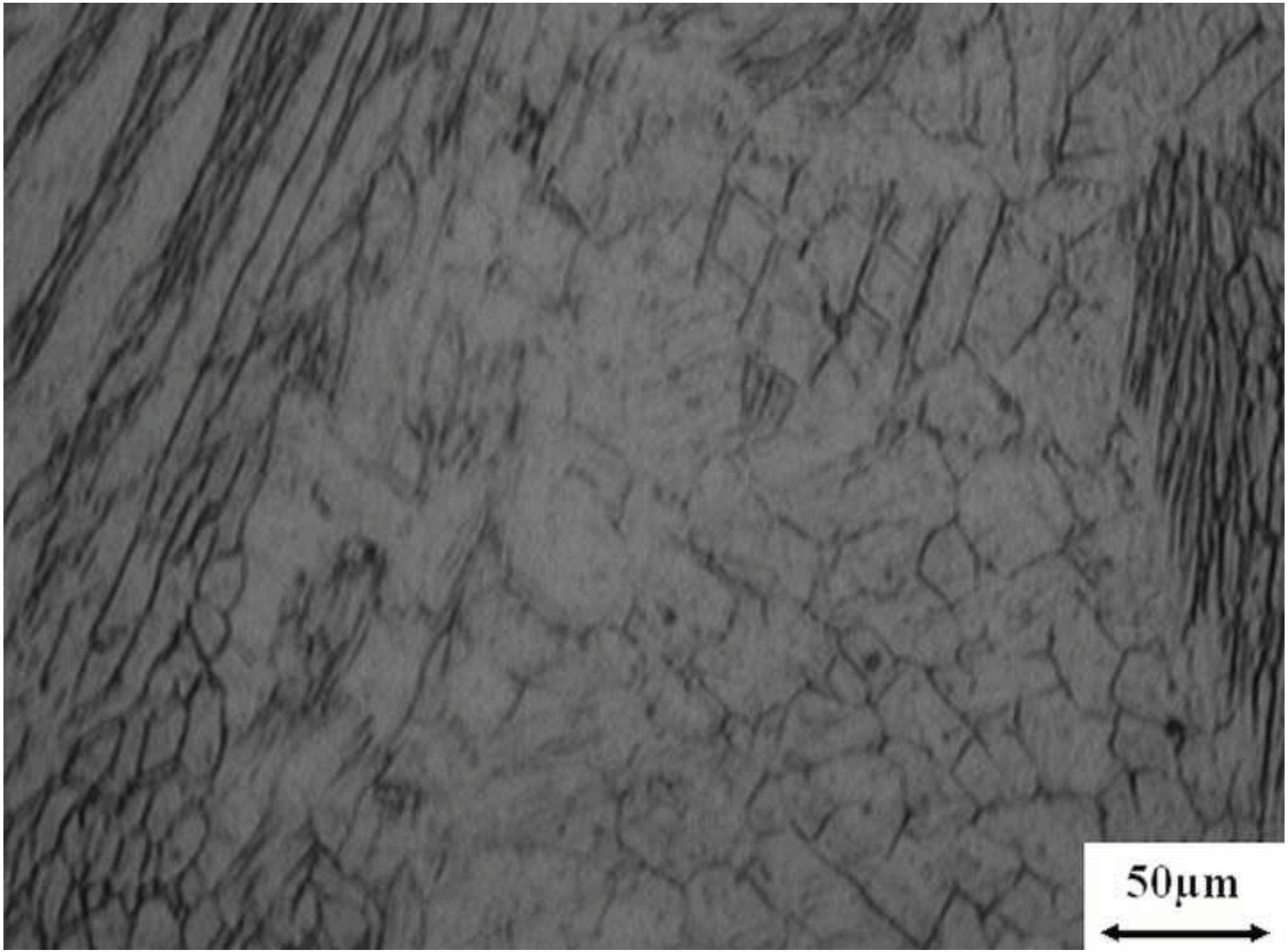

Figure 4b
Click here to download high resolution image

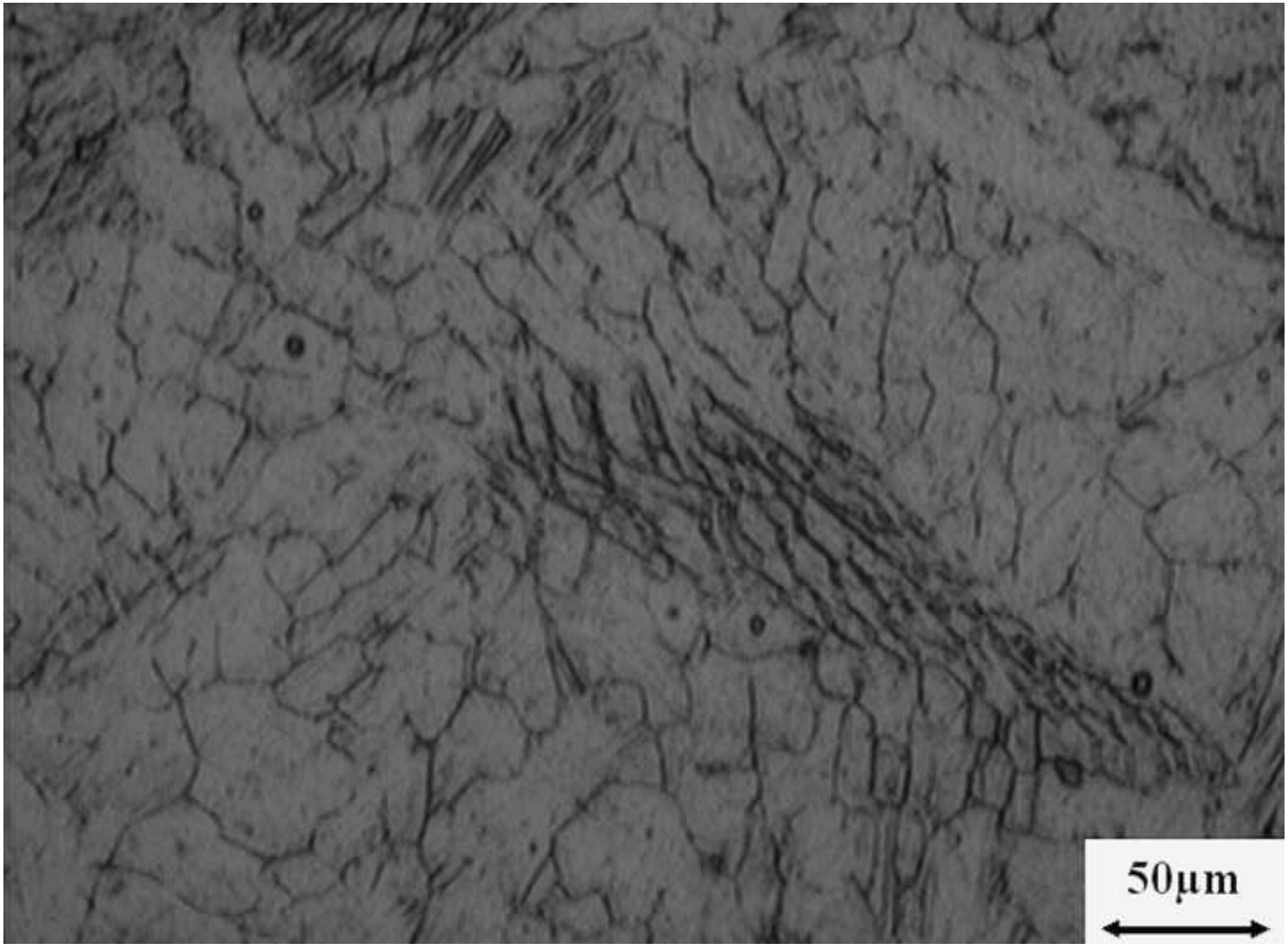

Figure 5
Click here to download high resolution image

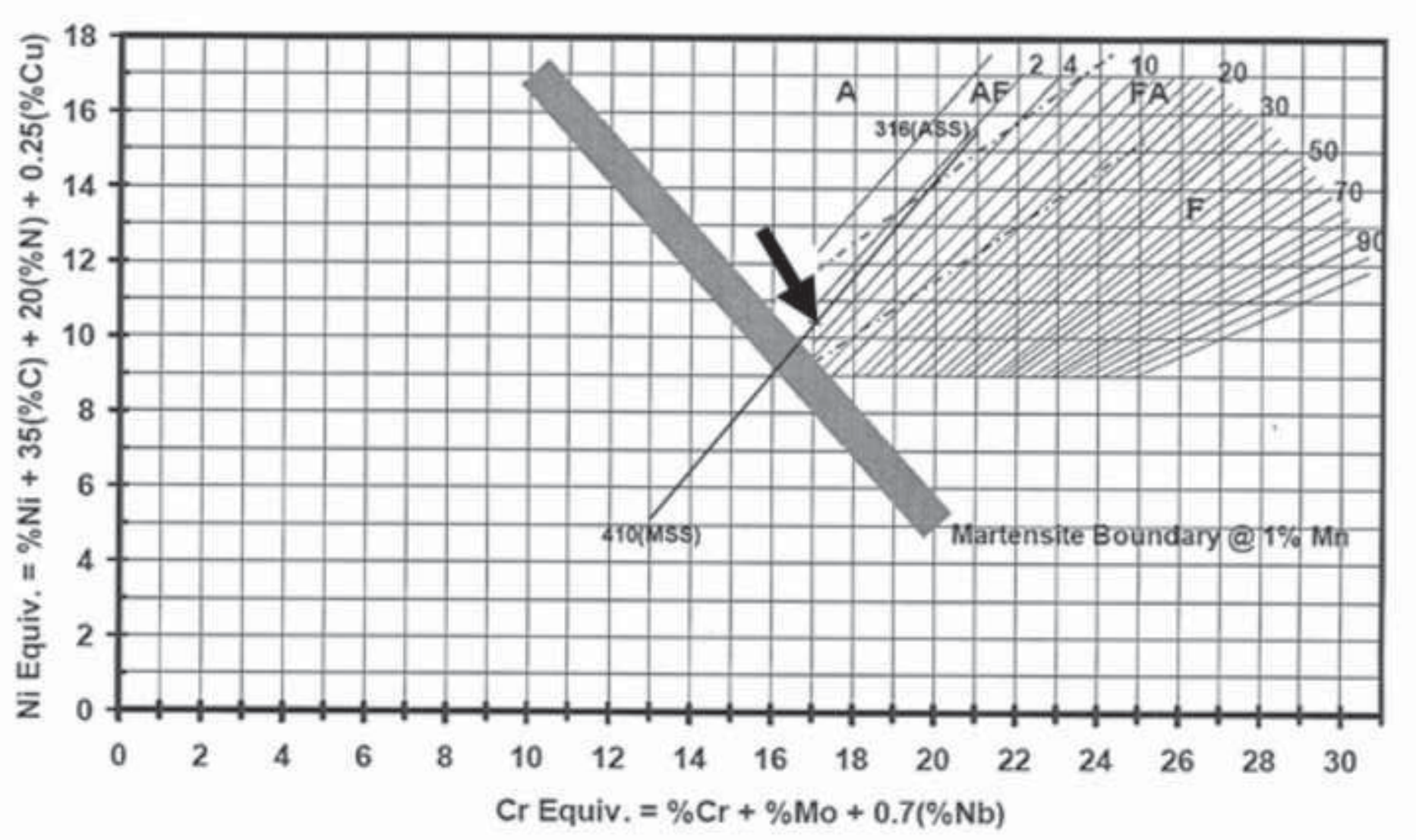

Figure 6
Click here to download high resolution image

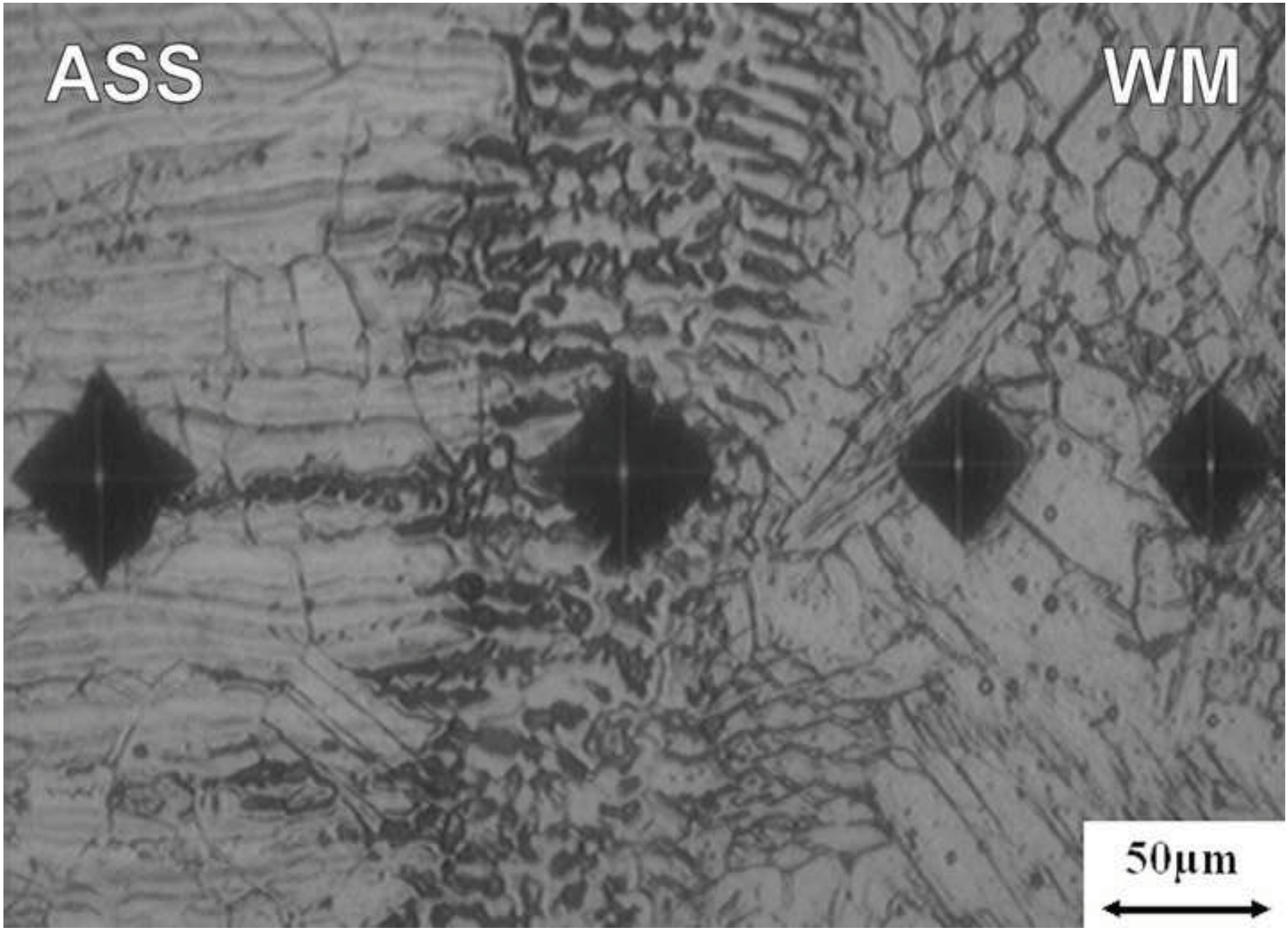

Figure 7
Click here to download high resolution image

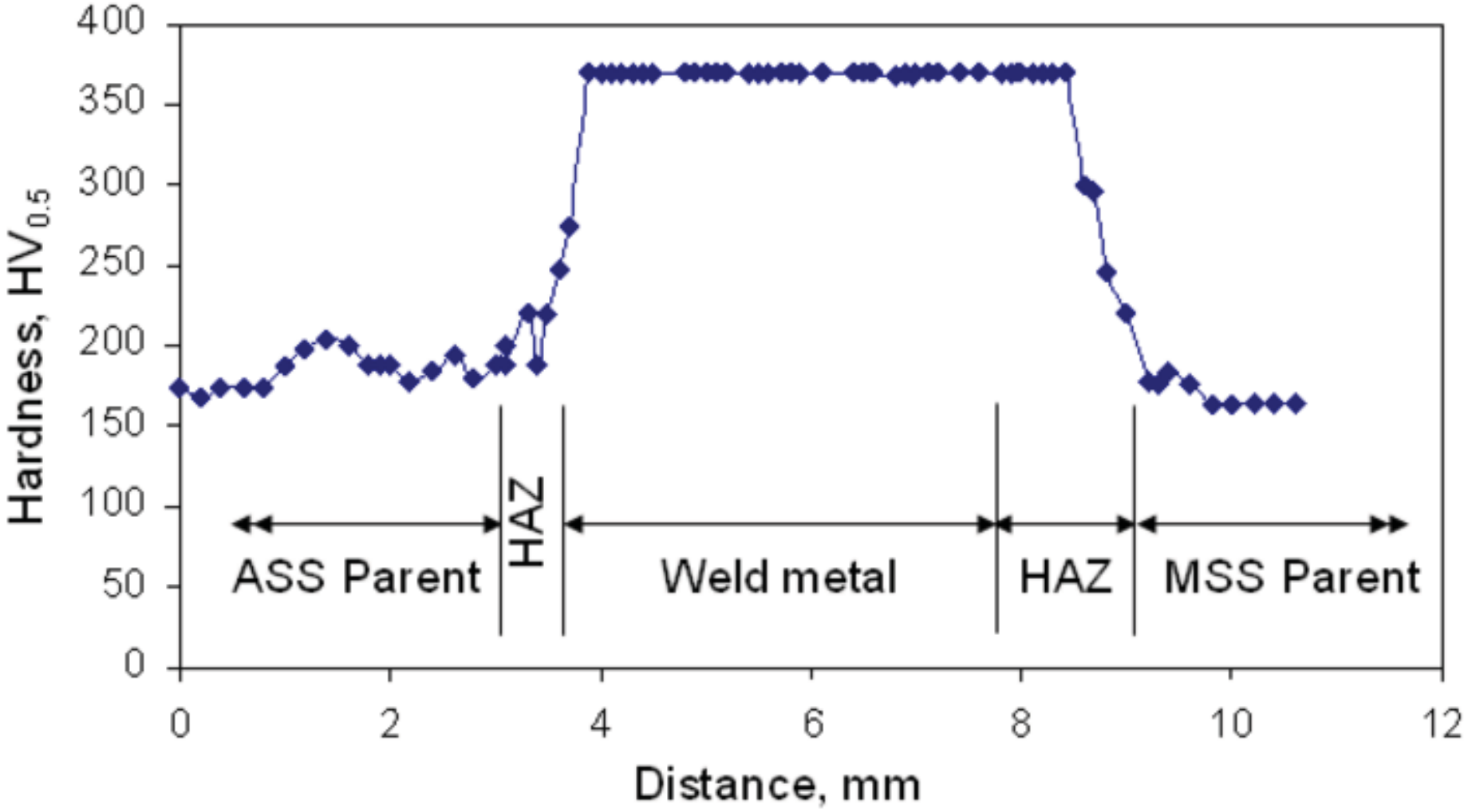

Figure 8a
Click here to download high resolution image

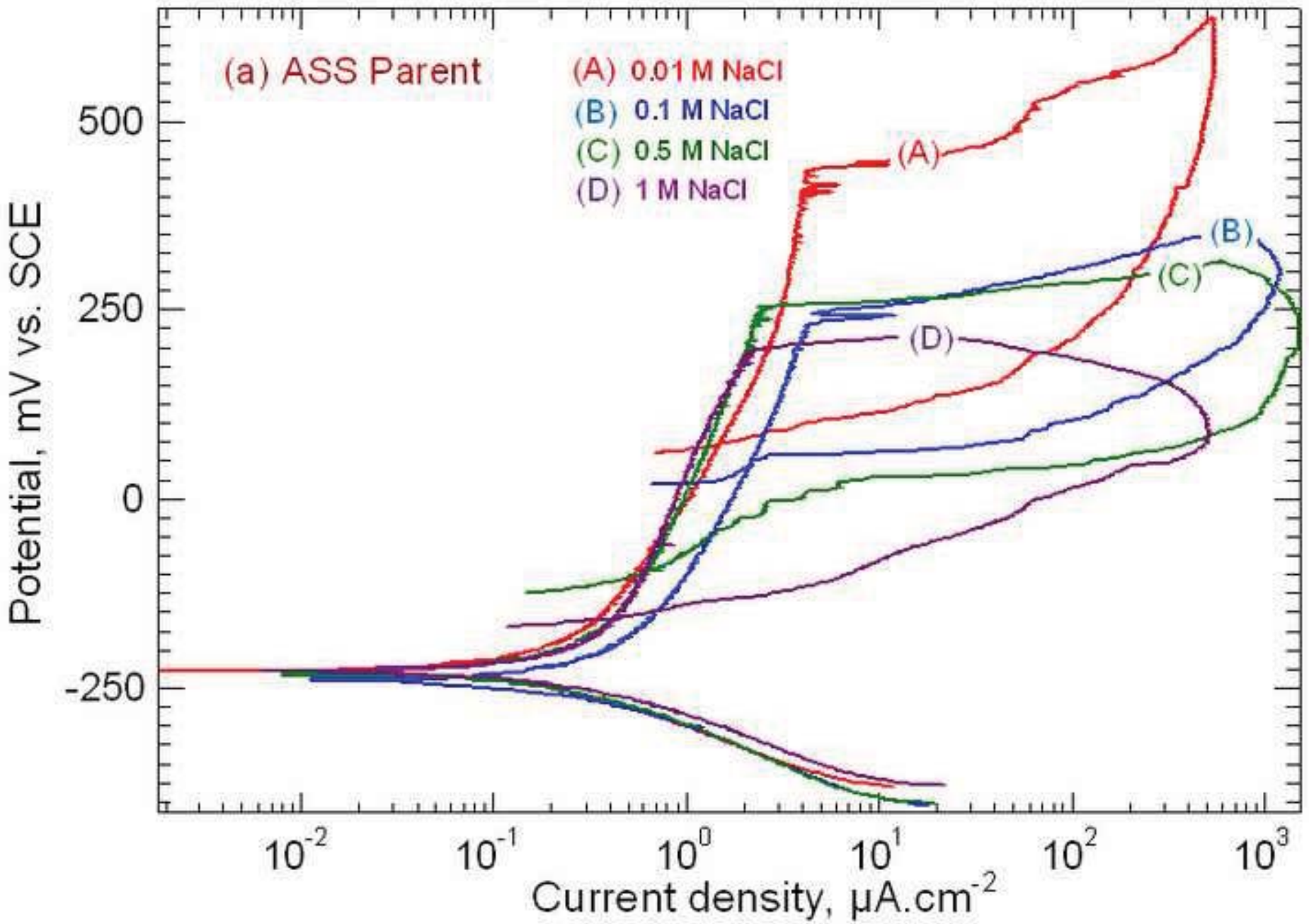

Figure 8b
Click here to download high resolution image

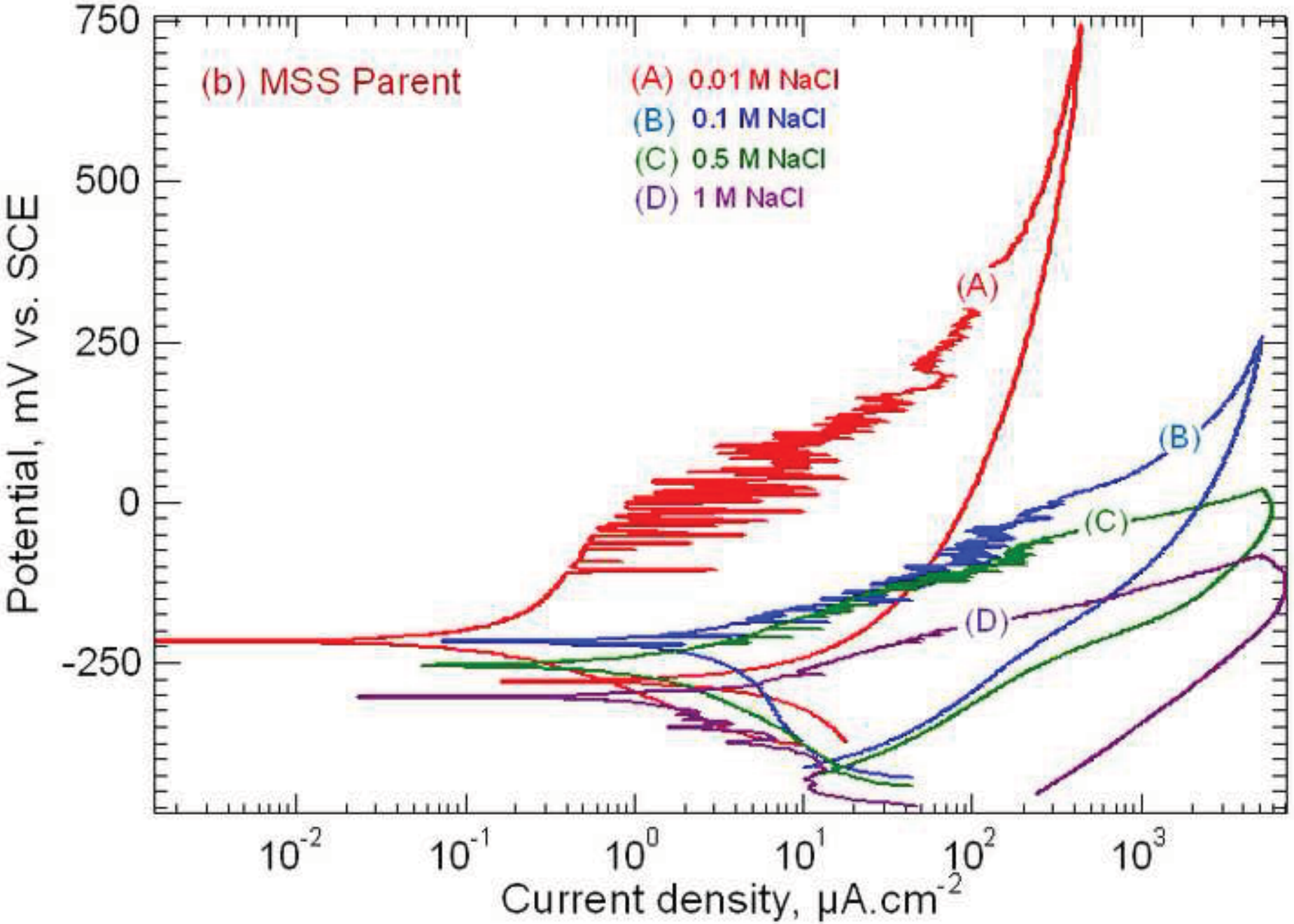

Figure 8c
Click here to download high resolution image

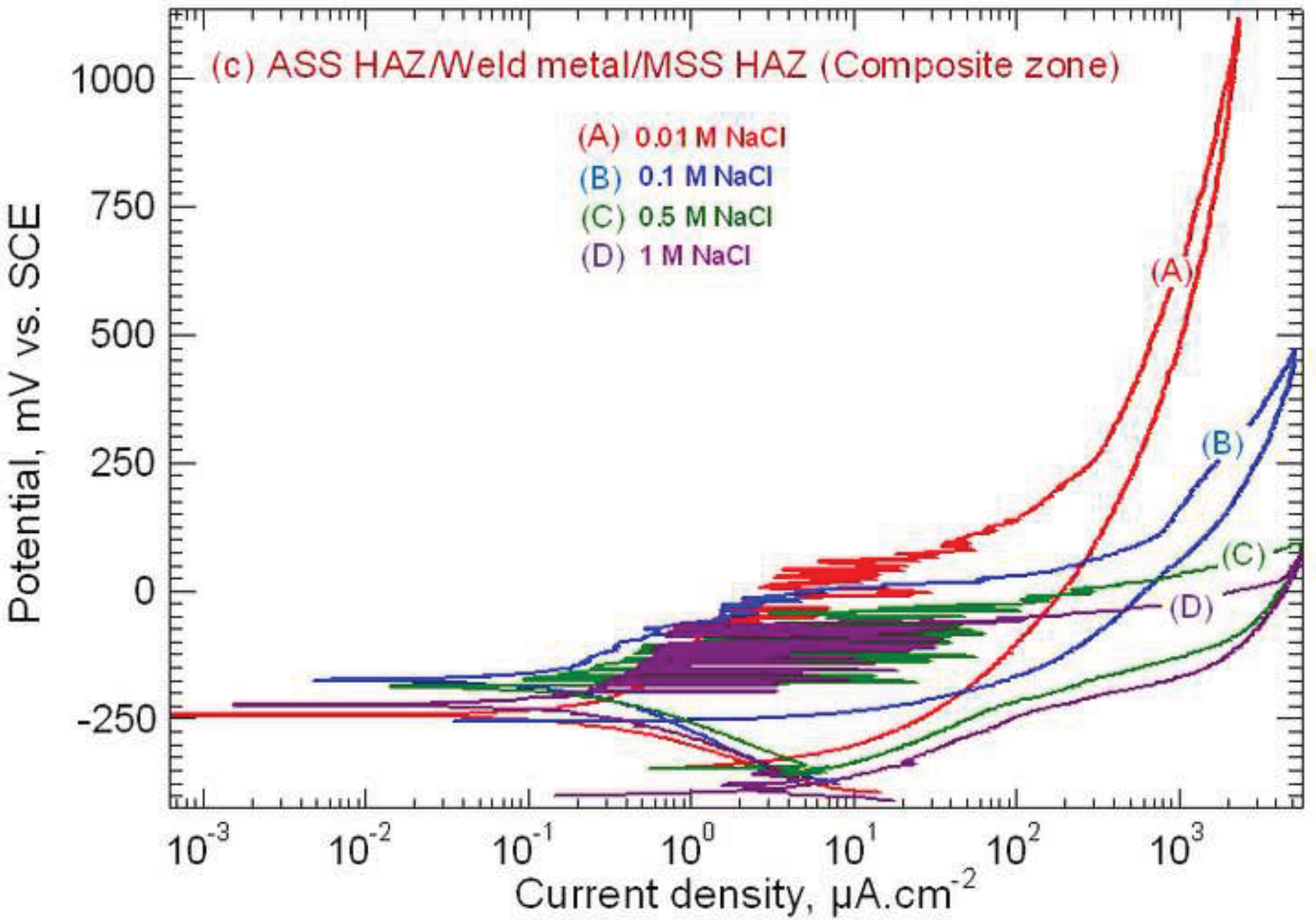

Figure 9a
Click here to download high resolution image

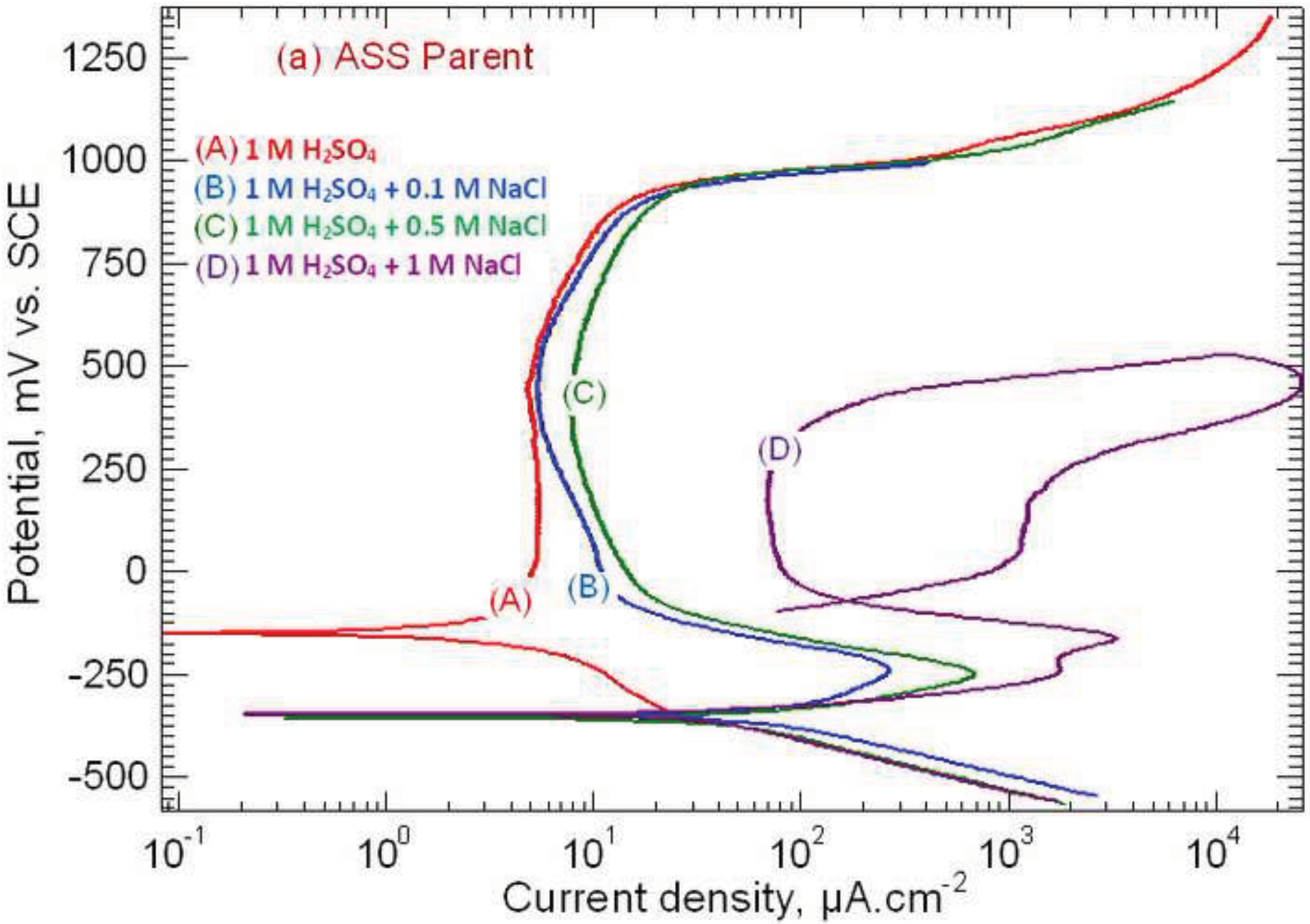

Figure 9b
Click here to download high resolution image

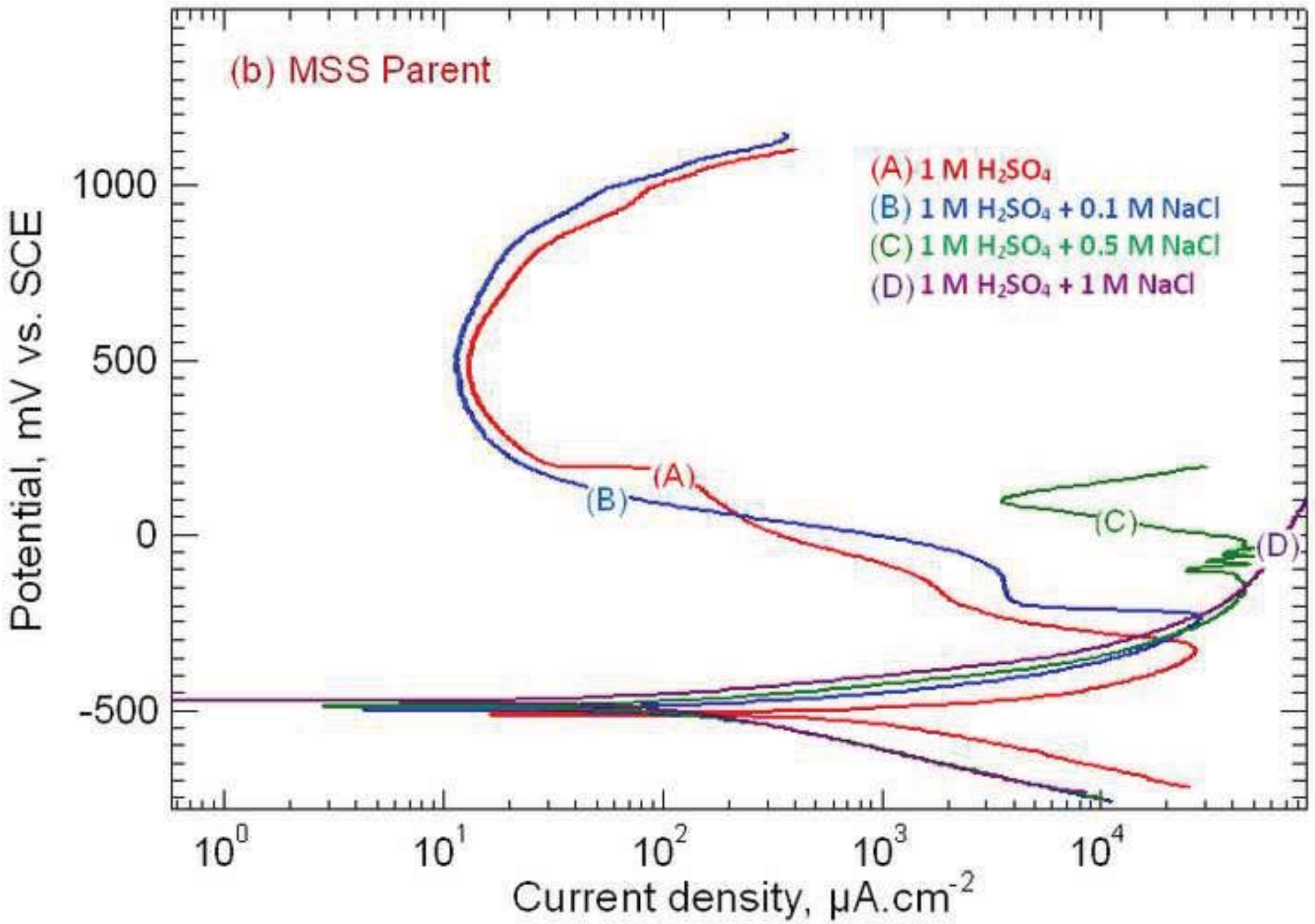

Figure 9c
Click here to download high resolution image

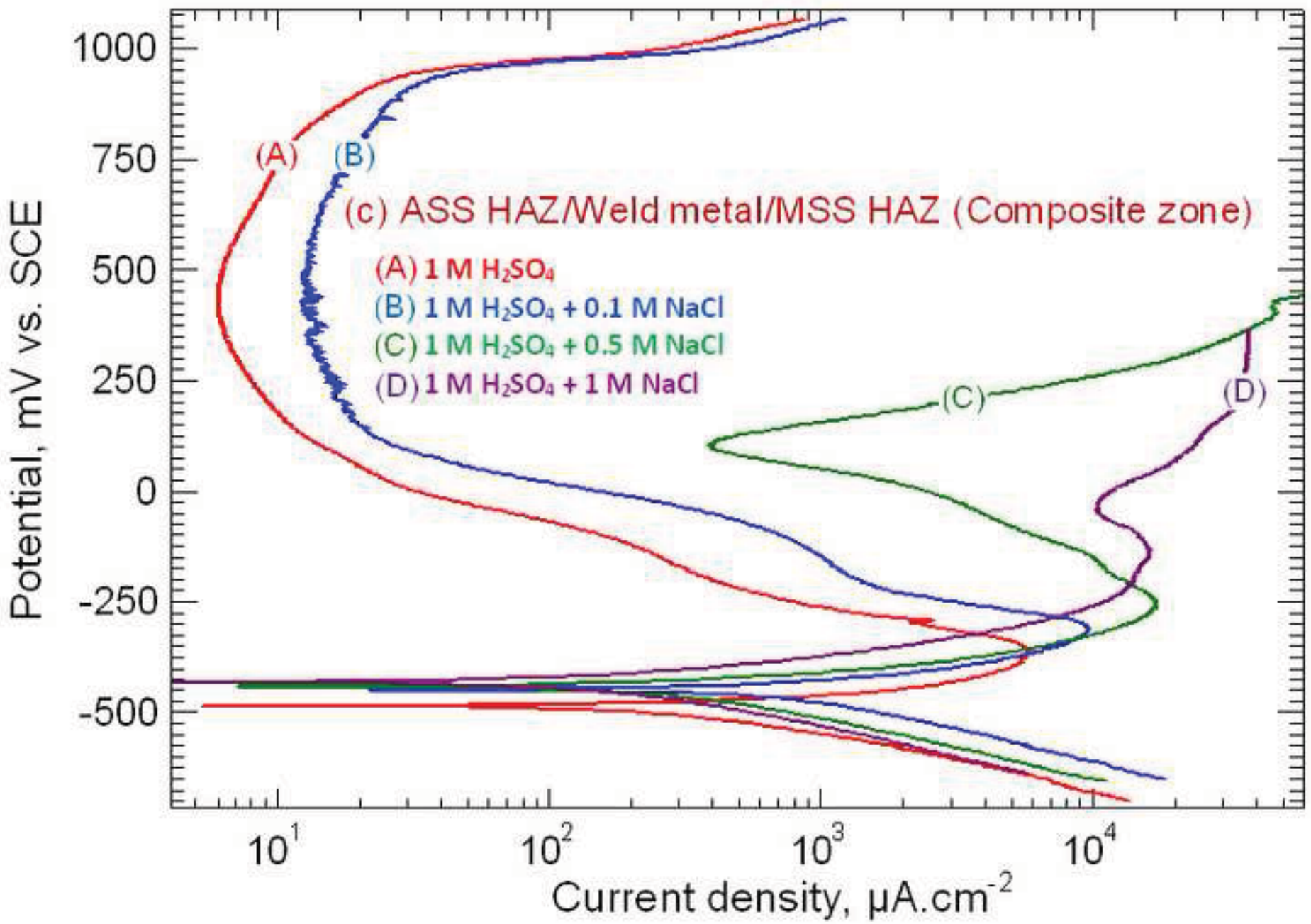

Figure 10
Click here to download high resolution image

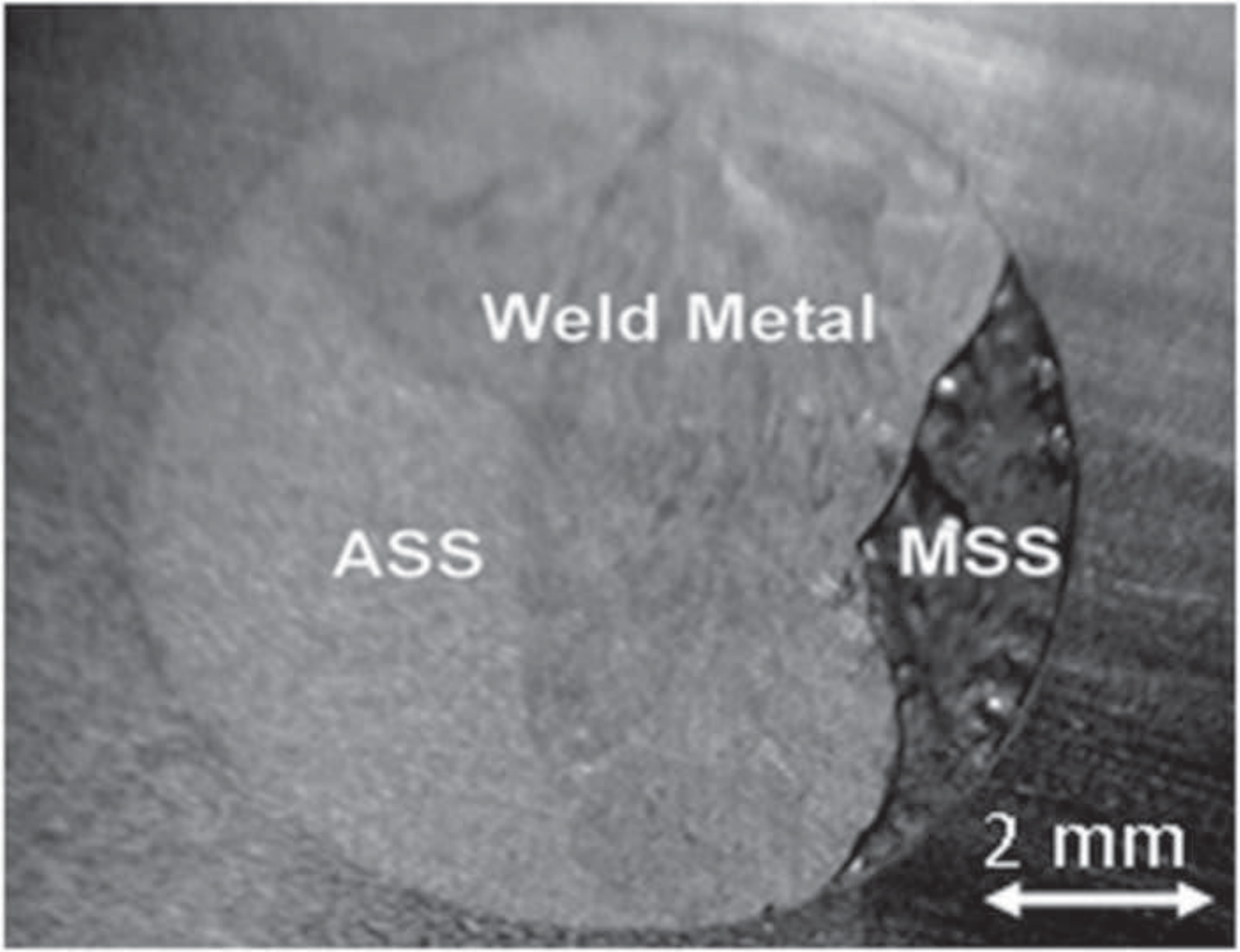

Figure 11a
Click here to download high resolution image

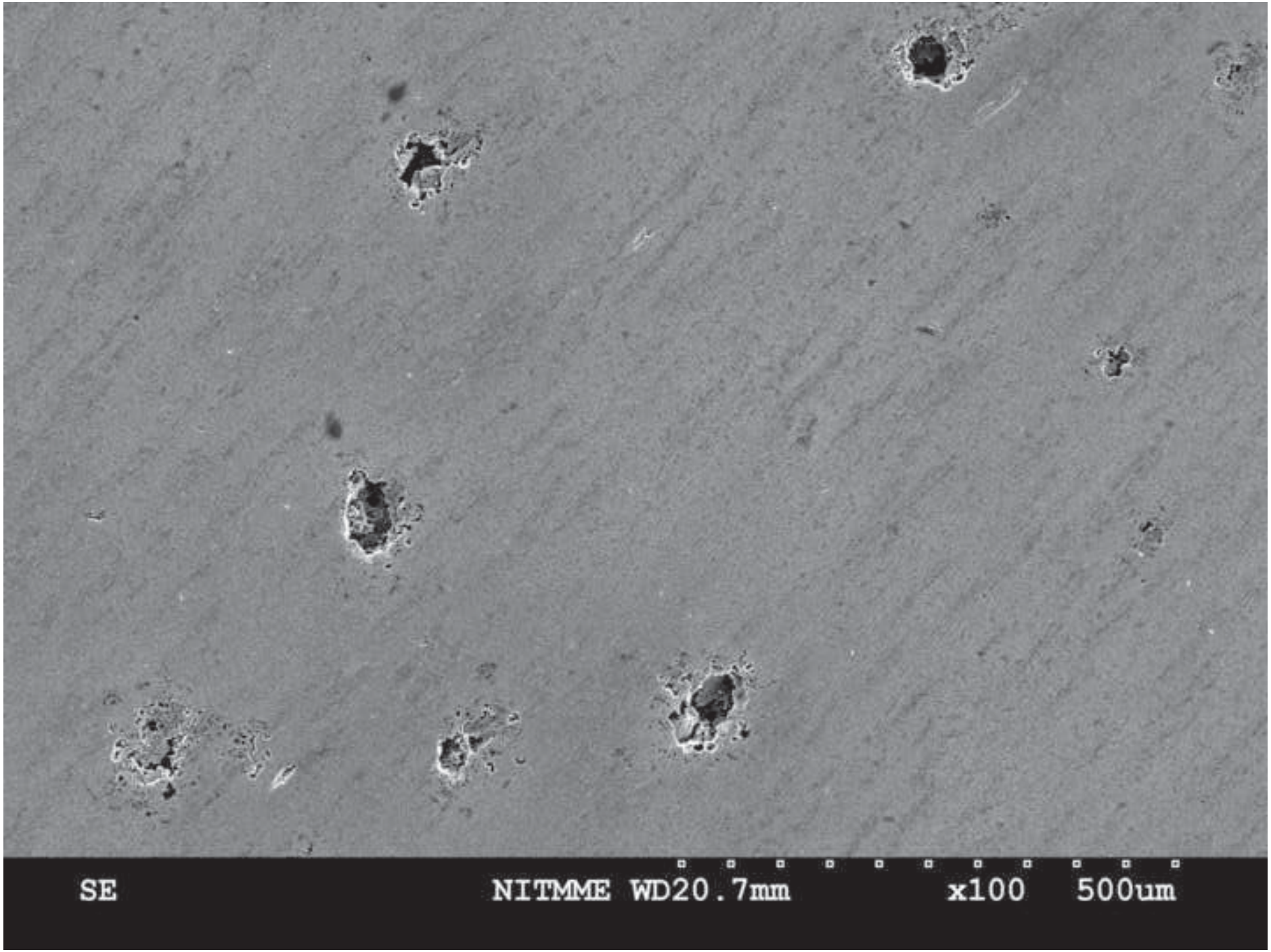

Figure 11b
Click here to download high resolution image

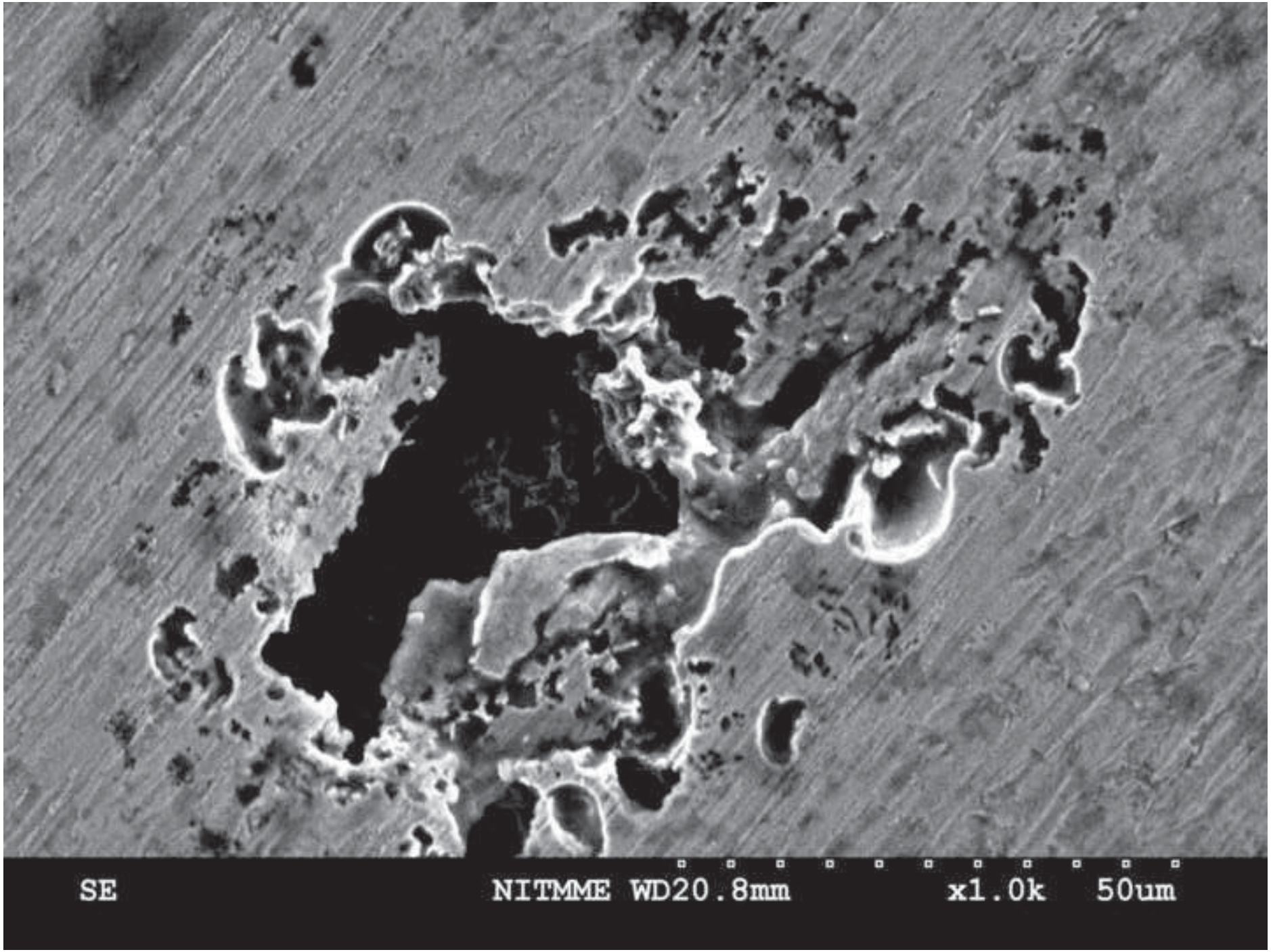

Figure 12
Click here to download high resolution image

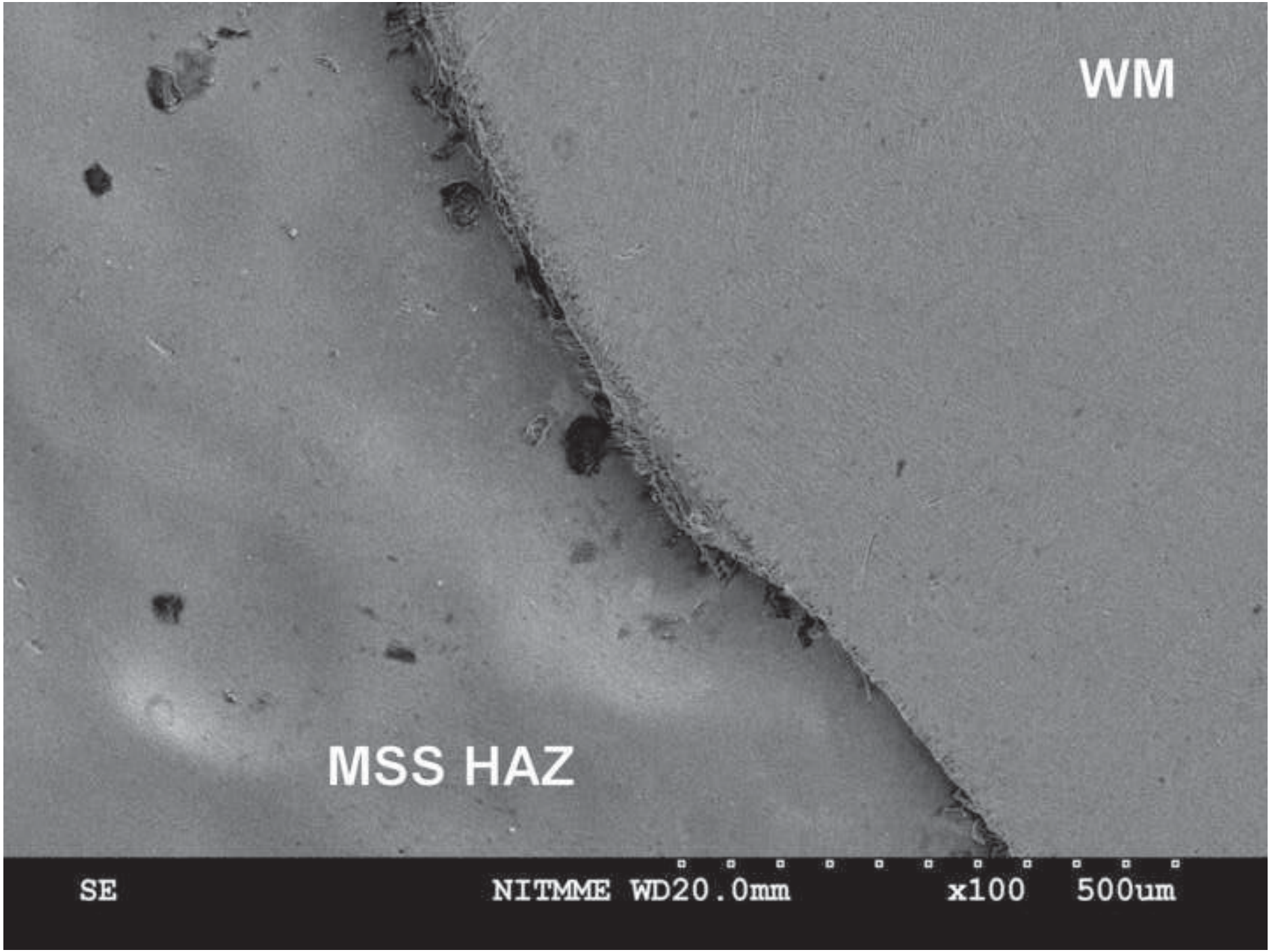

Figure 13
Click here to download high resolution image